White Rose Research Online

eprints@whiterose.ac.uk
https://eprints.whiterose.ac.uk
Universities of Leeds, Sheffield and York

Deposited via The University of Sheffield.

White Rose Research Online URL for this paper:
https://eprints.whiterose.ac.uk/id/eprint/147085/

Version: Accepted Version

Article:
Li, W., Xiao, Z., Cai, J. et al. (2019) Correlating the electron-donating core structure with morphology and performance of carbon-oxygen-bridged ladder-type non-fullerene acceptor based organic solar cells. Nano Energy, 61. pp. 318-326. ISSN: 2211-2855

https://doi.org/10.1016/j.nanoen.2019.04.053

Article available under the terms of the CC-BY-NC-ND licence (https://creativecommons.org/licenses/by-nc-nd/4.0/).

Reuse
This article is distributed under the terms of the Creative Commons Attribution-NonCommercial-NoDerivs (CC BY-NC-ND) licence. This licence only allows you to download this work and share it with others as long as you credit the authors, but you can't change the article in any way or use it commercially. More information and the full terms of the licence here: https://creativecommons.org/licenses/

Takedown
If you consider content in White Rose Research Online to be in breach of UK law, please notify us by emailing eprints@whiterose.ac.uk including the URL of the record and the reason for the withdrawal request.

UNIVERSITY OF LEEDS
University of Sheffield
UNIVERSITY of York

Correlating the Electron-donating Core Structure with Morphology and Performance of Carbon-Oxygen-Bridged Ladder-type Non-fullerene Acceptor based Organic Solar Cells

Wei Li[1,2], Zuo Xiao[3], Jinlong Cai[1,2], Joel A. Smith[4], Emma L. K. Spooner[4], Rachel C. Kilbride[4], Onkar S. Game[4], Donghui Li[1,2], Huijun Zhang[1,2], Mengxue Chen[1,2], Robert S. Gurney[1,2], Dan Liu[1,2], Richard A. L. Jones[4], David G. Lidzey[4*], Liming Ding[3*], Tao Wang[1,2]*

[1]School of Materials Science and Engineering, Wuhan University of Technology, Wuhan 430070, China E-mail: twang@whut.edu.cn

[2]State Key Laboratory of Silicate Materials for Architectures, Wuhan University of Technology, Wuhan 430070, China

[3]Center for Excellence in Nanoscience (CAS), Key Laboratory of Nanosystem and Hierarchical Fabrication (CAS), National Center for Nanoscience and Technology, Beijing 100190, China E-mail: ding@nanoctr.cn

[4]Department of Physics and Astronomy, University of Sheffield, Sheffield, S3 7RH, UK E-mail: d.g.lidzey@sheffield.ac.uk

Abstract: The chemical structure of non-fullerene acceptors (NFAs) affects their light-harvesting abilities, energy levels and molecular orders, all of which play a crucial role in determining the efficiency of organic solar cells (OSCs). In this work, we have systematically investigated a series of ladder-type NFAs having different carbon-oxygen-bridged electron-donating cores, and revealed the effects of core structures and film casting conditions on molecular ordering and performance of OSCs. We found that NFAs containing the thieno[3,2-b]thiophene centered, 6 or 8 fused rings (i.e. CO*i*6DFIC, CO*i*8DFIC) exhibit narrower optical band gaps than NFAs containing the benzene centered, 5 or 7 fused rings (i.e. CO*i*5DFIC, CO*i*7DFIC). NFAs containing less fused rings in the carbon-oxygen-bridged core (i.e. CO*i*5DFIC and CO*i*6DFIC) exhibit edge-on molecular orientation in the blends with face-on oriented PTB7-Th donor, and result in low device efficiency. Although NFAs containing extended fused rings (i.e. CO*i*7DFIC and CO*i*8DFIC) possess a pronounced flat-on lamellar crystalline structure in the pure state, the crystallization can be reduced after blending with PTB7-Th as well as by hot-substrate casting, while the lamella in CO*i*8DFIC can be effectively suppressed to form only face-on π–π stacks, which leads to enhanced PCE of OSCs.

Key words: organic solar cells; non-fullerene acceptors; molecular order; device efficiency

Introduction

Advances over the past few years have evidenced encouraging progress of organic solar cells (OSCs) employing non-fullerene, n-type conjugated molecules as electron acceptors [1-6], with the maximum power conversation efficiency (PCE) of over 15% having been achieved in single junction devices [7] and 17% has been reached in tandem devices [8], demonstrating a bright and promising future for OSCs. Among a number of driving forces to enable the rapid development of OSCs, the rise of non-fullerene electron acceptors (NFAs), including both fused-ring and non-fused-ring electron acceptors, plays a leading role[9-12]. Those fused-ring NFAs feature a coplanar molecular geometry consisting of two electron-deficient units linked by a fused-ring electron-rich core that are substituted with side chains [13-17]. With the manipulation of the core structure, the energy levels, absorption spectrum, carrier mobility and morphological features of NFAs can be tuned effectively [18-22]. Whilst there now exists a great understanding of how the chemical structures of the electron-donating cores will affect the energy levels and optical band gaps of NFAs, less is known about how they will influence the molecular ordering and morphologies in their photovoltaic blends [23-25].

The bulk heterojunction morphology of OSCs is one of the critical issues for achieving high device PCE, which originates from the chemical structure of NFAs and is highly related to the light absorption, exciton dissociation, charge recombination and charge transport processes [26-28]. In comparison to the conventional ball-like structured fullerene derivative acceptors, e.g. PCBM, the diverse structures of NFAs enable the formation of various molecular order and aggregation states in films processed under different conditions [29-31]. Consequently, the morphological configurations of NFA-based OSCs are sophisticated and more difficult to optimize [32-35]. Recently, novel NFAs featuring the carbon-oxygen-bridged (C-O-bridged) core unit were developed and have demonstrated high efficiency in both single junction and tandem OSCs [8, 36-39]. These C-O-bridged electron-donating cores enhance the electron-donating capability and molecular planarity, leading to narrower bandgaps and stronger light-harvesting capability of NFAs [40]. More interestingly, our previous work has demonstrated that the molecular order of the 8 fused-ring based C-O-bridged NFA, i.e. CO*i*8DFIC, can be adjusted from edge-on and flat-on lamella to H- and J- type π-π stacking to broaden the absorption spectrum by casting the photovoltaic blend on a hot substrate [31].

In this work, we have studied a series of NFAs having the same electron-accepting groups on two sides but different C-O-bridged electron-donating cores, and found that the molecular ordering

and optoelectronic properties in the pure NFAs and their photovoltaic solar cells are highly related to the electron-donating core structures as well as the film-processing conditions. Results show that the thieno[3,2-b]thiophene centered NFAs (i.e. CO*i*6DFIC and CO*i*8DFIC) have narrower optical band gaps compared to the benzene-centered NFAs (i.e. CO*i*5DFIC and CO*i*7DFIC). Moreover, NFAs containing fewer fused rings in the C-O-bridged core (i.e. CO*i*5DFIC and CO*i*6DFIC) exhibit edge-on orientation in the blends with face-on oriented PTB7-Th donor, and result in low PCE of the device. Although NFAs containing extended fused rings (i.e. CO*i*7DFIC and CO*i*8DFIC) show pronounced flat-on lamellar crystalline structure in the pure state, the crystallization can be reduced after blending with PTB7-Th as well as by hot-substrate casting, with the lamella in CO*i*8DFIC effectively suppressed to form face-on π–π stacks only, which leads to enhanced PCE of OSCs.

Results and Discussion

The chemical structures of CO*i*XDFIC (X=5, 6, 7 or 8) NFAs are shown in **Figure 1a**. All these NFAs carry two 2-(5,6-difluoro-3-oxo-2,3-dihydro-1H-inden-1-ylidene)malononitrile units as the electron-deficient terminal groups and four hexylbenzene units as side chains attached to the core structures. The principal structural difference between these four NFAs is their C-O-bridged electron-donating core unit. CO*i*5DFIC and CO*i*7DFIC are centered with a benzene ring, whilst CO*i*6DFIC and CO*i*8DFIC are centered with a thieno[3,2-b]thiophene group, then thiophene and thieno[3,2-b]thiophene groups are fused on both sides via the carbon-oxygen-bridges to form 5, 6, 7 or 8 fused rings in the electron-donating core and resulting in CO*i*5DFIC, CO*i*6DFIC, CO*i*7DFIC or CO*i*8DFIC respectively. The energy levels of these NFAs are shown in **Figure 1b**, where it is seen that CO*i*7DFIC exhibits upshifted highest occupied molecular orbital (HOMO) and lowest unoccupied molecular orbital (LUMO) of 0.18 and 0.25 eV respectively compared to CO*i*5DFIC, whilst CO*i*8DFIC exhibits upshifted HOMO and LUMO levels of 0.14 and 0.18 eV respectively compared to CO*i*6DFIC. This suggests that the HOMO and LUMO energy levels of CO*i*XDFIC can be upshifted by extending the thiophene units alongside the centering unit. These CO*i*XDFIC molecules were dissolved in chlorobenzene solution and cast at room temperature (RT) or on a 100 °C heated hot substrate (HS) to enable a prolonged or shortened molecular organization time respectively, and therefore varied molecular ordering, during the film drying process (**Figure 1c**)[41,42].

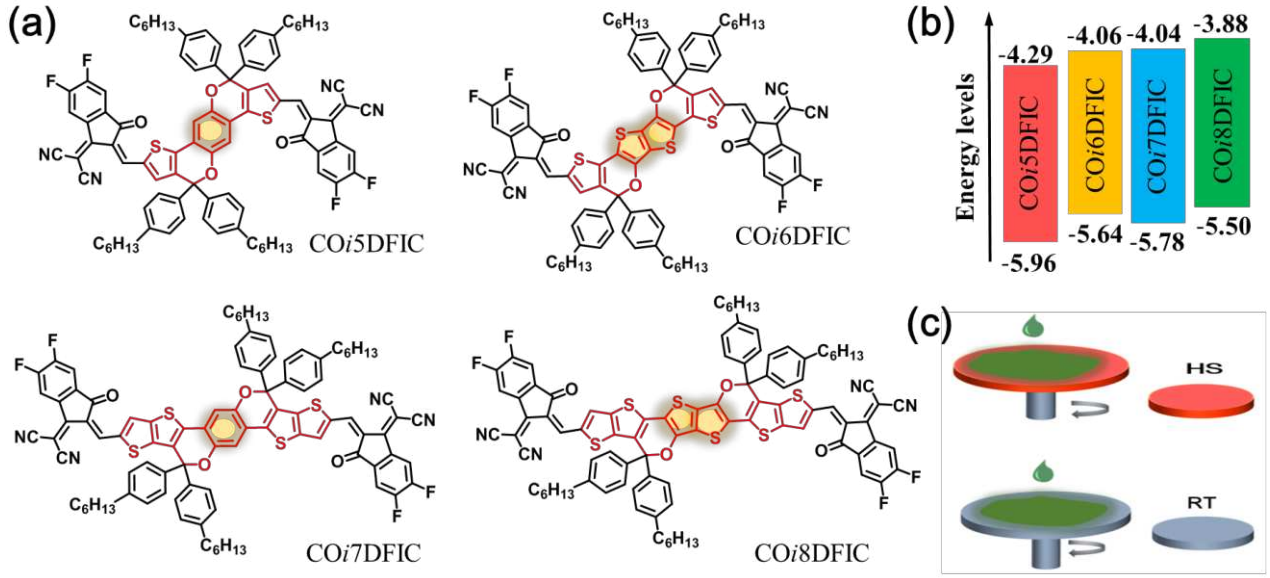

Figure 1 (a) Chemical structure and (b) energy levels of CO*i*XDFIC materials (X= 5, 6, 7 or 8), (c) Schematic of film-casting on a substrate held at room temperature (RT) or on a hot substrate (HS).

The absorption (Abs.) and photoluminescence (PL) spectra of CO*i*XDFIC solutions and films are shown in **Figure 2**. In a solution state, the benzene-centered CO*i*5DFIC and CO*i*7DFIC show an intramolecular charge transfer band (ICT) from *ca.* 550-750 nm, and give the maximum absorption peaks at 670 and 683 nm respectively. The thieno[3,2-b]thiophene-centered CO*i*6DFIC and CO*i*8DFIC exhibit stronger ICT at *ca.* 600-850 nm, and give maximum absorption peaks at 760 and 773 nm respectively. After all CO*i*XDFIC solutions were cast onto films at RT, the absorption spectra of CO*i*5DFIC and CO*i*7DFIC films red-shifted 30 and 34 nm, resulting in similar optical band gaps of 1.56 and 1.55 eV respectively (calculated from the offset of the absorption spectrum). However, for the thieno[3,2-b]thiophene-centered NFAs, CO*i*6DFIC and CO*i*8DFIC exhibit significant red-shifts of 62 and 80 nm, corresponding to much narrower optical band gaps of 1.31 and 1.26 eV respectively. This absorption spectra study suggests that although the extended thiophene rings alongside the C-O-bridged core structure can enhance the ICT and reduce the optical band gap of NFAs slightly, the centering unit of these ladder-type NFAs is the determining factor for the ICT and optical band gap characteristics.

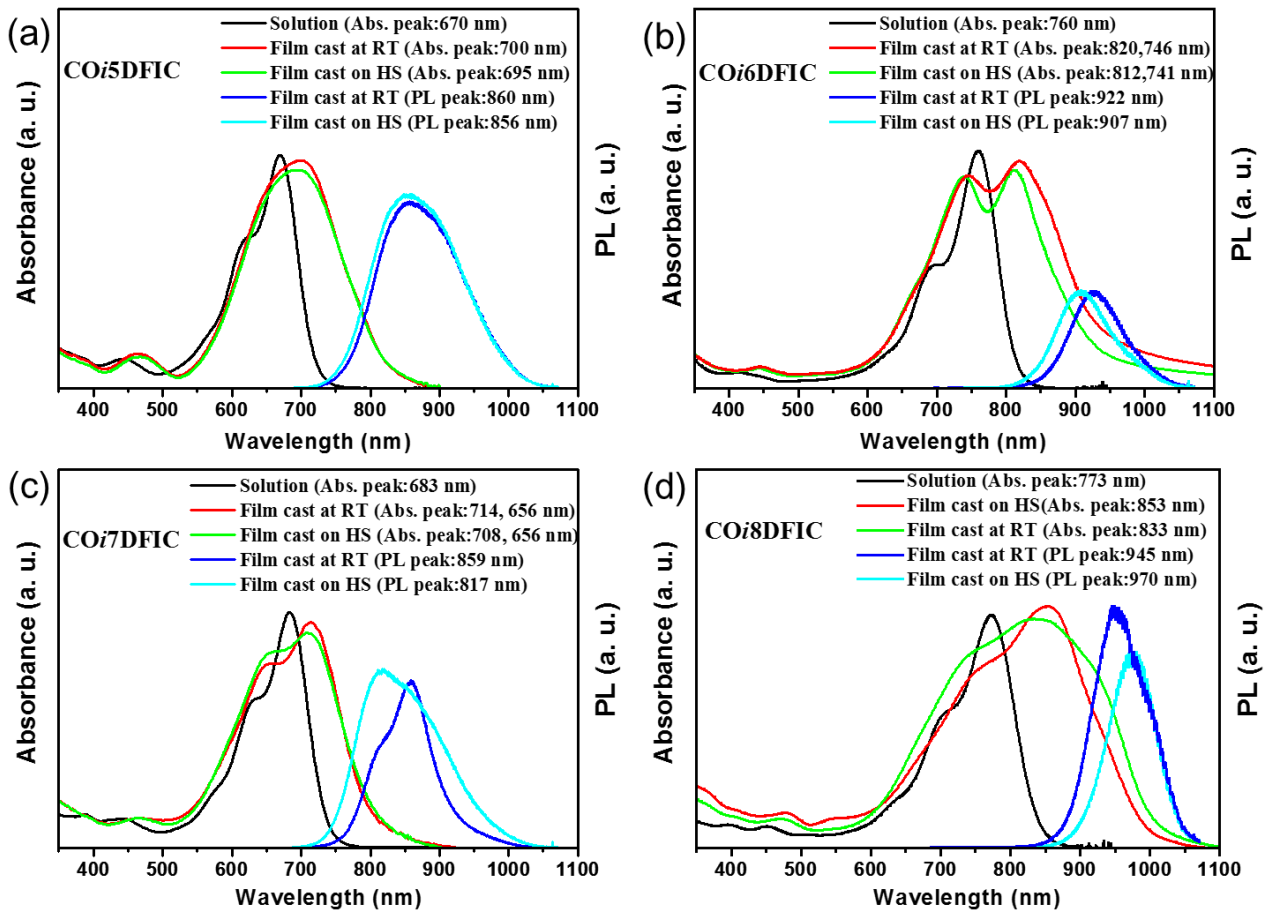

Figure 2 Absorption spectra of CO*i*XDFIC in a chlorobenzene solution, and CO*i*XDFIC films cast at RT and on HS. PL spectra of CO*i*XDFIC films cast at RT and on a hot substrate (HS).

Specifically, with the least amount of fused rings in the C-O bridged core, the CO*i*5DFIC film cast at RT exhibits a broad absorption band peaking at 700 nm. When the HS method was applied to cast the film, both absorption and PL spectra exhibit negligible difference, indicating that the condensed state of CO*i*5DFIC molecules in the solid film does not vary with different film-casting conditions. For CO*i*6DFIC, the film cast at RT exhibits two pronounced peaks at 746 and 820 nm, which correlate to the H- and J- type π-π stacks in the film respectively [43]. After the HS method was applied, the two absorption peaks blue-shift to 741 and 812 nm, and this blue-shift is also evidenced in the PL spectrum. HS casting therefore reduces the molecular ordering in the CO*i*6DFIC film, especially the J-aggregation. For CO*i*7DFIC, the film cast at RT possesses a strong vibronic peak at 714 nm with another weaker peak at 656 nm, indicating that the J-type π-π stacking overwhelms the H-type π-π stacking. When HS casting was applied, the location of these vibronic peaks remains constant, but the intensity of the two peaks changed with the lower wavelength peak reducing and higher wavelength peak increasing in intensity, suggesting the transformation from J-type aggregates

to H-type aggregates. The enhanced H-type aggregation also leads to the enhanced PL intensity at shorter wavelength. For CO*i*8DFIC, the film cast at RT possesses the broadest absorption spectrum among all four NFAs here, with a primary peak located at 853 nm and less pronounced shoulders on either side that can be correlated to H- and J- type π-π stacks in the solid film[31]. When HS casting was applied, the intensity of the primary peak reduces but the intensities of two shoulders both increase, suggesting enhanced H- and J- type π-π stacks. The overall effect of the enhanced H- and J-type π-π stacks in CO*i*8DFIC thin film is the slight increase and red-shift of the PL peak from 980 to 945 nm.

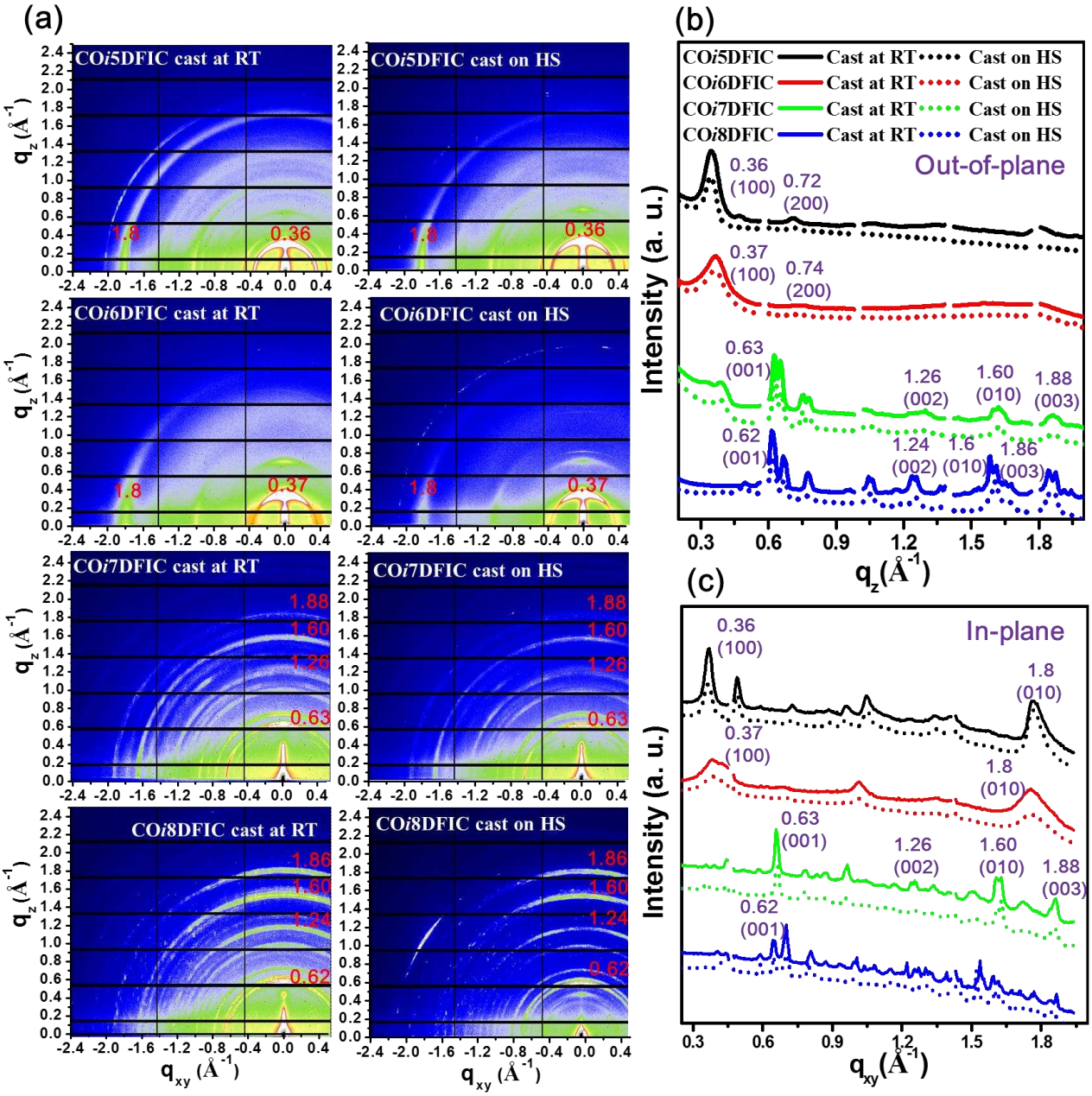

Figure 3 (a) 2D GIWAXS patterns of CO*i*XDFIC films cast at RT or on HS. (b) Out-of-plane and (c) in-plane 1D profiles of CO*i*XDFIC films cast at RT and on HS.

The 2D grazing-incidence wide-angle X-ray scattering (GIWAXS) patterns and 1D profiles of CO*i*XDFIC films cast at RT or on HS are shown in **Figure 3**. For CO*i*5DFIC and CO*i*6DFIC films cast at RT, the (100) diffraction rings of both NFAs are located at q=0.36 $Å^{-1}$ and 0.37 $Å^{-1}$ respectively and are preferentially stronger in the out-of-plane direction (q_z axis). The (010) π-π stacking peaks are observed at q=1.8 $Å^{-1}$ along the in-plane direction (q_{xy} axis). These features correspond to a typical edge-on oriented lamellar crystalline structure. When HS was used to cast CO*i*5DFIC and CO*i*6DFIC films, these features largely remain with only slightly reduced intensities of some diffraction signals. Furthermore, the optical microscope images of CO*i*XDFIC films cast at RT or on HS are shown in **Figure S1**. It can be found that both CO*i*5DFIC and CO*i*6DFIC films exhibit uniform and continuous surface morphology whether they were cast at RT or on HS, suggesting that they possess good film-forming abilities which are not sensitive to the film-casting conditions. Compared to the distinct edge-on lamellar feature in pure CO*i*5DFIC and CO*i*6DFIC films, the GIWAXS images of pure CO*i*7DFIC and CO*i*8DFIC films cast at RT exhibit numerous sharp diffraction rings located from q=0.5 to 2 $Å^{-1}$ along both q_z and q_{xy} directions, implying that CO*i*7DFIC and CO*i*8DFIC molecules are highly crystallized in their films. Due to their pronounced crystallization ability, CO*i*7DFIC and CO*i*8DFIC films cast at RT present large aggregates with long aspect ratios on the film surface (see **Figure S1**). Among the diffraction rings in the GIWAXS images, the (001), (002) and (003) diffraction rings of CO*i*7DFIC film respectively locate at q_z=0.63, 1.26 and 1.88 $Å^{-1}$, and those of CO*i*8DFIC locate at q_z=0.62, 1.24, 1.86 $Å^{-1}$, corresponding to the backbone stacking of flat-on lamellar crystals. These results not only imply that the poor film-forming properties of CO*i*7DFIC and CO*i*8DFIC could originate from their pronounced backbone stacking, but also suggest that the expanded C-O bridged core structure (fused 7 or 8 rings) can favor the backbone stacking and enhance the crystallinity of NFAs [44]. Unlike CO*i*5DFIC and CO*i*6DFIC, whose (010) π-π stacking is preferentially stronger in the in-plane direction, the (010) π-π stacking of RT-cast CO*i*7DFIC and CO*i*8DFIC are ring-like and appear strong in both in-plane and out-of-plane directions. Meanwhile, when HS was applied to cast CO*i*7DFIC and CO*i*8DFIC films, the intensities of various diffraction rings all decrease, consistent with our previous report that casting films on HS can shorten the molecular self-organization time and result in reduced crystallinity [31,41]. Encouragingly, it can be found that the large aggregates on the HS-cast CO*i*8DFIC film surface all disappeared and the film appears uniform and continuous, although the CO*i*7DFIC film still possesses small aggregates on the surface (**Figure S1**). This leads us to conclude that HS casting is effective at retarding the strong

crystallization of CO*i*8DFIC, but less effective on CO*i*7DFIC in aiding preparation of a uniform film.

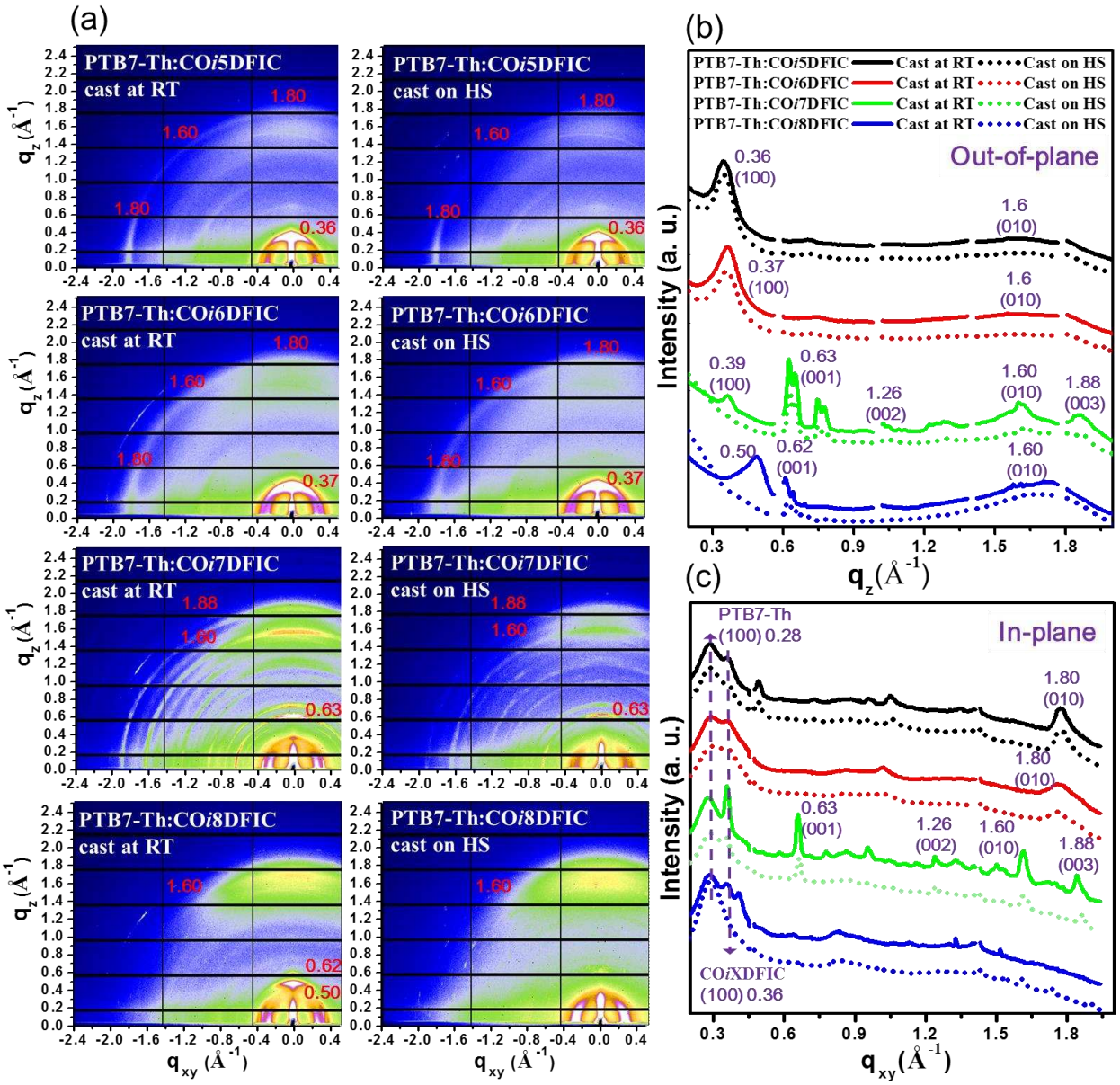

Figure 4 (a) 2D GIWAXS patterns of PTB7-Th:CO*i*XDFIC films cast at RT and on HS. (b) Out-of-plane and (c) in-plane 1D profiles of GIWAXS patterns of PTB7-Th:CO*i*XDFIC films cast at RT and on HS.

We further investigated the molecular ordering features of these CO*i*XDFIC NFAs in their photovoltaic blends with the electron donor PTB7-Th. The mass ratio of PTB7-Th to CO*i*XDFIC was fixed at 1:1.5 in all films for a fair comparison in this study, although our previous work has shown that the optimum blend ratios varied slightly [31]. The 2D GIWAXS patterns and 1D profiles of PTB7-Th:CO*i*XDFIC films cast at RT or on HS are shown in **Figure 4**, and their corresponding optical microscopy, scanning probe microscopy (SPM) and transmission electron microscopy (TEM) images

are shown in **Figures S2, S3 and S4**, respectively. In all PTB7-Th:CO*i*XDFIC films, PTB7-Th presents face-on oriented morphology with the (010) peak locating at q_z=1.6 Å^{-1} and the (100) peak locating at q_{xy}=0.28 Å^{-1}, demonstrating that the molecular order and orientation of PTB7-Th do not alter after blending with CO*i*XDFIC. The molecular orientation of the acceptor in the PTB7-Th:CO*i*5DFIC and PTB7-Th:CO*i*6DFIC films cast at RT remains edge-on, with their (100) and (010) diffraction patterns being stronger in the in-plane and out-of-plane directions respectively. The crystallization of CO*i*5DFIC and CO*i*6DFIC was interrupted due to the presence of PTB7-Th (by comparing Figures 3 and 4), which can be judged from the reduced intensities of various diffraction patterns in the blends, however it was insensitive to RT or HS casting. This is supported by the similar surface morphology of the PTB7-Th:CO*i*5DFIC and PTB7-Th:CO*i*6DFIC films cast at RT or on HS shown in **Figure S2** and **Figure S3** (demonstrating low root mean square (RMS) surface roughnesses lower than 2 nm). High resolution TEM images in Figure S4 also show nanoscale phase separation that is in principle beneficial to exciton dissociation and charge transport.

While the strong flat-on lamellar crystallization of CO*i*7DFIC was not inhibited after blending with PTB7-Th nor by HS casting, this is achieved in the PTB7-Th:CO*i*8DFIC blends. This is supported by the GIWAXS characterizations, with pronounced diffraction rings present in both RT and HS cast PTB7-Th:CO*i*7DFIC films but reduced significantly in the RT and HS cast PTB7-Th:CO*i*8DFIC films. The failure to inhibit the lamellar crystallization of CO*i*7DFIC in the PTB7-Th:CO*i*7DFIC blend by either RT or HS casting results in large CO*i*7DFIC aggregates in the blend films as seen in the optical images in Figure S2, SPM images in Figure S3, as well as TEM images in Figure S4. The inhibition of flat-on lamellar crystallization with the addition of PTB7-Th was observed to be more effective in CO*i*8DFIC. While the backbone stacking (at *ca.* q_z=0.62 Å^{-1}) and alky chain stacking (at q_z=0.5 Å^{-1}) of CO*i*8DFIC exist in the RT-cast PTB7-Th:CO*i*8DFIC film, their intensities reduce significantly and the film appears uniform and homogenous with no large aggregates on the surface (see Figure S2 and S3). The aggregates were completely inhibited by applying HS casting for the PTB7-Th:CO*i*8DFIC blend, with both surface SPM and bulk TEM images showing fine nanoscale phase separation. The most obvious feature of the GIWAXS characterization of HS-cast PTB7-Th:CO*i*8DFIC film is the preferential face-on π–π stacking at q_z=1.6 Å^{-1}, which is now the same orientation with the electron donor PTB7-Th. The molecular orientations of electron donors and acceptors in the same direction have been found to enhance the charge dissociation efficiency and charge transport of PTB7-Th:CO*i*8DFIC solar cells in our previous

report.[31]

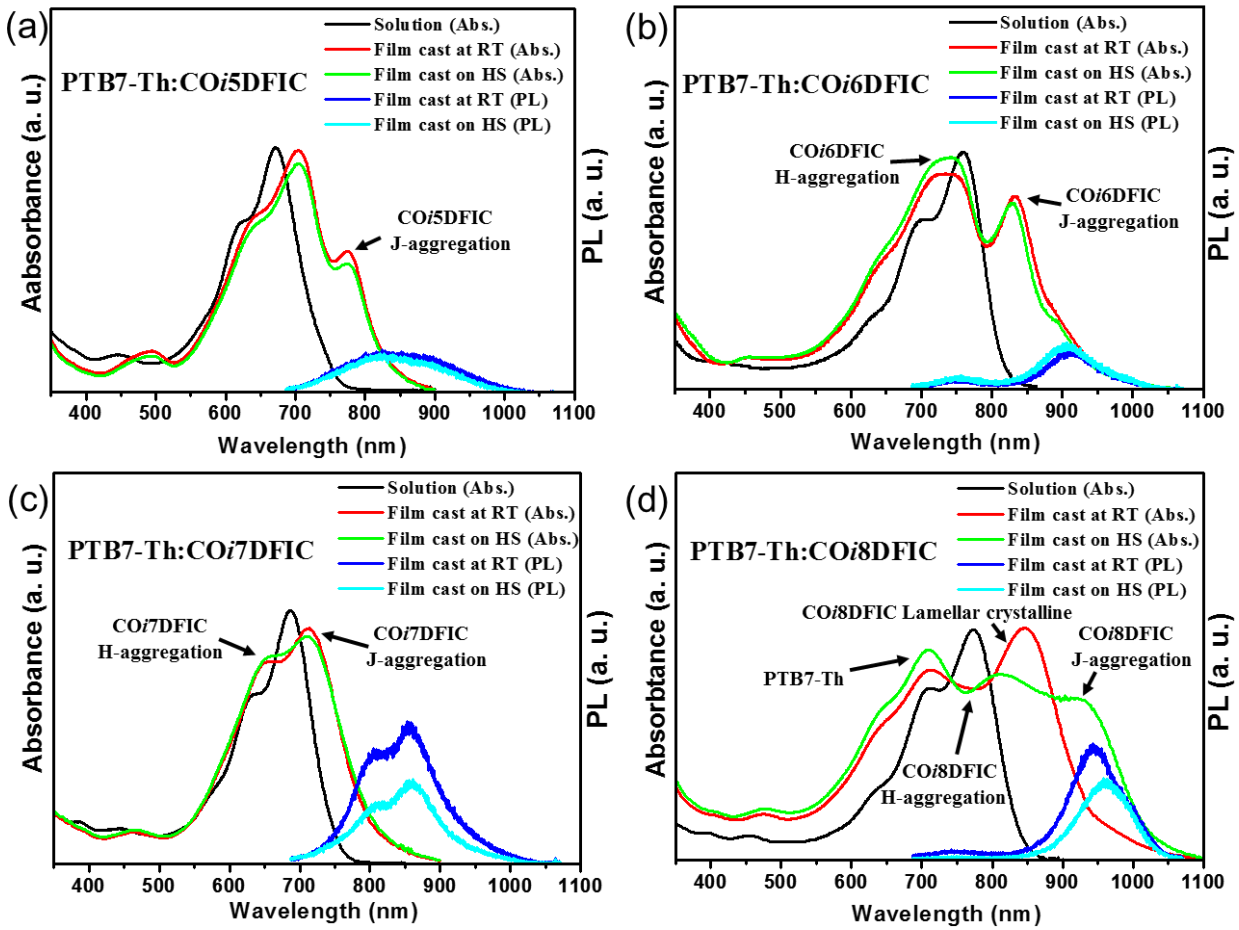

Figure 5 Absorption spectra of PTB7-Th:CO*i*XDFIC chlorobenzene solutions, PTB7-Th:CO*i*XDFIC films cast at RT and on HS (left axis). The PL spectra of PTB7-Th:CO*i*XDFIC films cast at RT and on HS (right axis).

The absorption and PL spectra of PTB7-Th:CO*i*XDFIC films cast at RT or on HS are shown in **Figure 5**. Similar to the pure CO*i*5DFIC film, PTB7-Th:CO*i*5DFIC films cast at RT or on HS exhibit limited difference in their absorption and PL spectra. Moreover, although the absorption spectrum of PTB7-Th (PTB7-Th film possesses a vibronic peak at 710 nm with a shoulder around 680 nm) largely overlaps with that of pure CO*i*5DFIC film, and distinct peaks around 776 nm emerge in the absorption spectra of PTB7-Th:CO*i*5DFIC blend films cast at RT and on HS. The appearance of these peaks indicates the formation of the J-type π-π stacking of CO*i*5DFIC in the blend films. By comparing with spectra presented in Figure 2a, we can conclude that the condensed state of CO*i*5DFIC is hardly altered by varying the film-casting temperature but can be modified by blending with PTB7-Th. Similar to pure CO*i*6DFIC films cast at RT or on HS, the PTB7-Th:CO*i*6DFIC film cast at RT and on HS also exhibits two characteristic peaks at 741 and 835 nm, and HS casting increases the peak

that is associated with H-type π–π stacking in the blend, and there is a marginal blue-shift in the PL spectrum. Furthermore, the PL intensities of PTB7-Th:CO*i*5DFIC and PTB7-Th:CO*i*6DFIC films cast at RT or on HS are similar, suggesting that the PL quenching efficiency in the film, and consequently the size of phase separated donors and acceptors domains did not alter upon different processing conditions [45]. For the PTB7-Th:CO*i*7DFIC blend, the film cast on HS exhibits an increased peak at 650 nm but a decreased peak at 710 nm, suggesting enhanced H-type stacking but reduced J-type π–π stacking, a trend that is similarly found in the pure CO*i*7DFIC film. However, for the PTB7-Th:CO*i*8DFIC blend, the film cast on HS shows enhanced J-type and H-type π-π stacking compared to its film cast at RT (see Figure 4), and results in broadened absorption and red-shifted PL spectra, consistent with our previous work [31]. Furthermore, with the reduced crystallinity and smaller phase separation sizes in the blend films, both PTB7-Th:CO*i*7DFIC and PTB7-Th:CO*i*8DFIC films cast on HS exhibit reduced PL intensities compared to the films cast at RT, suggesting more efficient PL quenching due to fine mixing of donors and acceptors in the blend films [46].

In order to evaluate the impact of different molecular order and optoelectronic properties of PTB7-Th:CO*i*XDFIC films on the device performance of corresponding OSCs, we have fabricated OSCs with an inverted device structure of ITO/ZnO/PTB7-Th:CO*i*XDFIC/MoO_3/Ag. The mass ratio of PTB7-Th to CO*i*XDFIC was also fixed at 1:1.5 for fair comparison. **Figure 6** plots the J-V curves and external quantum efficiency (EQE) spectra of champion devices, and **Table 1** summarizes the device metrics. Meanwhile, the exciton dissociation and charge collection processes in these OSCs were studied by investigating their photocurrent density versus effective voltage curves (Shown in **Figure S5** and **Table S1**). With a narrow absorption spectrum from 300-800 nm and contrasting molecular orientations between donor and acceptor in the photoactive layer, the RT-cast PTB7-Th:CO*i*5DFIC device exhibits a low saturated short-circuit current density (J_{sat}) of 15.8 mA cm^{-2}, low exciton dissociation efficiency (P_{diss}) of 90.8%, and poor charge collection efficiency (P_{coll}) of 65.1%. The inefficient exciton dissociation and charge collection processes render a low PCE of 4.5% associating with a V_{oc} of 0.59 V, FF of 52.7%, and J_{sc} of 14.4 mA cm^{-2}. Although the PTB7-Th:CO*i*6DFIC device also possesses the unfavorable contrasting orientation of donor and acceptor in the photoactive layer and attained a poor value of P_{coll} (lower than 80%), the RT-cast device achieved a PCE of 7.6%, mainly due to the much higher J_{sat} of 21.2 mA cm^{-2} and J_{sc} of 20.2 mA cm^{-2} as a result of the broader absorption spectrum (*ca.* 500-1000 nm, see Figure 5b). Meanwhile, it was found that PTB7-Th:CO*i*5DFIC and PTB7-Th:CO*i*6DFIC devices cast on HS exhibit similar or even slightly

reduced efficiency compared to the devices cast at RT, suggesting that the raised film-casting temperature does not improve the performance of these two systems. When using HS to cast the PTB7-Th:CO*i*7DFIC film to reduce its crystallinity and phase separation size, its P_{diss} and P_{coll} both increased from 90.4% and 62.0% to 94.1% and 86.0% respectively, suggesting improved exciton dissociation and charge collection processes. Consequently, the maximum FF, J_{sc} and PCE of HS-cast device were improved to 70.3%, 18.4 mA cm^{-2} and 8.7% respectively from 52.4%, 16.5 mA cm^{-2} and 5.8% of the RT-cast device. The PTB7-Th:CO*i*8DFIC device possesses the broadest absorption spectrum with the same face-on orientated π–π stacking of donor and acceptor in the photoactive layer. This favored morphological and optoelectronic features enable its RT-cast device to achieve a high J_{sat} of 25.6 mA cm^{-2}, with the P_{diss} of 95.4% and P_{coll} of 79.9%, associating with a high PCE of 10.9%, FF of 63.2%, J_{sc} of 24.5 mA cm^{-2} and V_{oc} of 0.70 V. Furthermore, when casting the film on HS to enhance its π-π stacking, the J_{sat}, P_{diss} and P_{coll} were improved to 28.1 mA cm^{-2}, 95.7%, and 83.2%, and resulted in the highest PCE of 13.1%, with the J_{sc} of 26.9 mA cm^{-2} and FF of 71.3%.

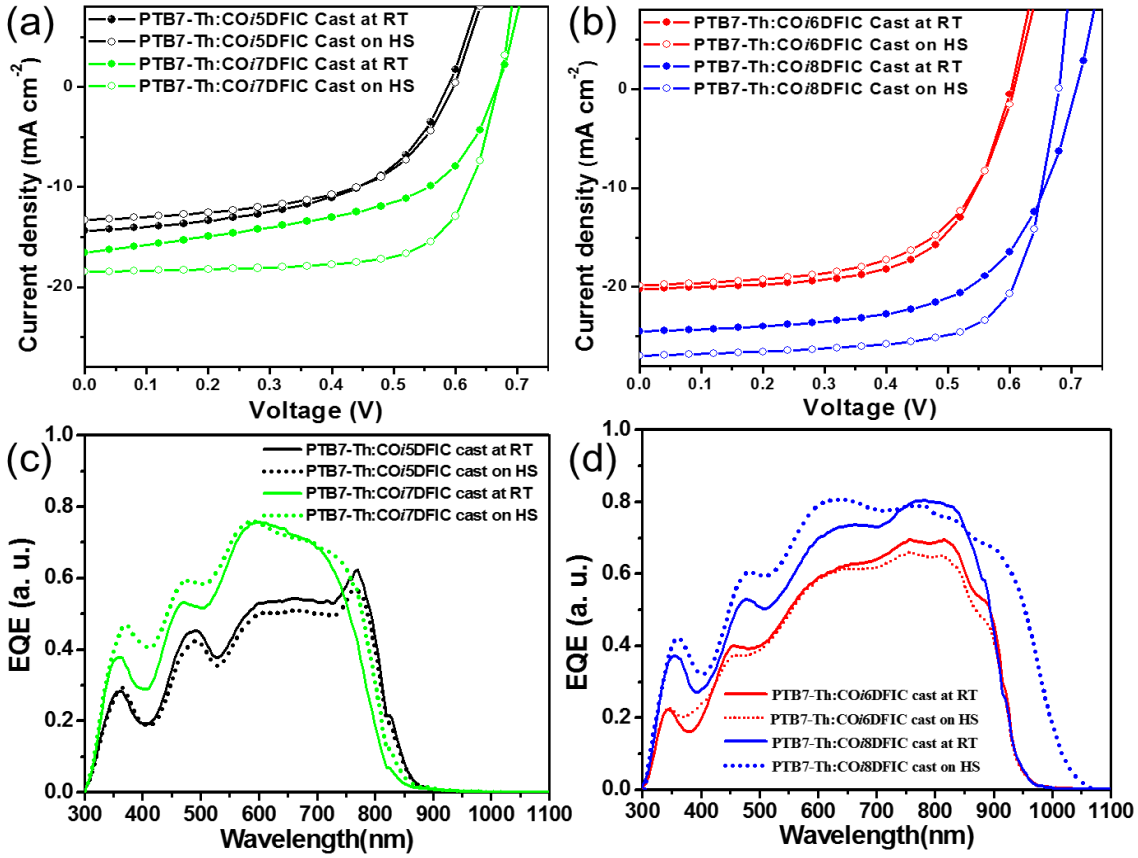

Figure 6 J-V and EQE curves of PTB7-Th:CO*i*5DFIC, PTB7-Th:CO*i*6DFIC, PTB7-Th:CO*i*7DFIC and PTB7-Th:CO*i*8DFIC devices with the photoactive layer cast at RT and on HS.

Table 1 Summary of photovoltaic parameters of OSCs measured at an illumination of AM 1.5G at 100 mW cm^{-2}. The statistical data presented here are averages obtained from 30 individual devices.

	FF [%]	J_{sc} [mA cm^{-2}]	Calculated J_{sc} from EQE [mA cm^{-2}]	V_{oc} [V]	PCE_{max} (PCE_{avg}) [%]
PTB7-Th:CO*i*5DFIC cast at RT	52.7	14.4	13.5	0.59	4.5 (4.3±0.2)
PTB7-Th:CO*i*5DFIC cast on HS	55.5	13.3	12.3	0.59	4.4 (4.1±0.2)
PTB7-Th:CO*i*6DFIC cast at RT	62.5	20.2	19.1	0.60	7.6 (7.2±0.3)
PTB7-Th:CO*i*6DFIC cast on HS	60.2	19.7	18.8	0.60	7.2 (6.9±0.2)
PTB7-Th:CO*i*7DFIC cast at RT	52.4	16.5	15.4	0.67	5.8 (5.1±0.5)
PTB7-Th:CO*i*7DFIC cast on HS	70.3	18.4	17.5	0.67	8.7 (8.2±0.3)
PTB7-Th:CO*i*8DFIC cast at RT	63.2	24.5	23.5	0.70	10.9 (10.3±0.4)
PTB7-Th:CO*i*8DFIC cast on HS	71.3	26.9	25.7	0.68	13.1 (12.7±0.2)

We also evaluated the voltage losses of PTB7-Th:CO*i*XDFIC devices fabricated via differing conditions. The optical bandgap (E_g) of PTB7-Th:CO*i*XDFIC blend films for evaluating voltage losses here was estimated as the energy at the intersection of the normalized absorptance and PL spectra [47]. Following the relationship of $V_{loss} = E_g - V_{oc}$, the V_{loss} values of RT-cast PTB7-Th:CO*i*5DFIC, PTB7-Th:CO*i*6DFIC, PTB7-Th:CO*i*7DFIC, PTB7-Th:CO*i*8DFIC devices were determined to be 1.04, 0.82, 0.95 and 0.67 V respectively (summarized in **Table S2**), suggesting that devices employing CO*i*XDFIC NFAs centered with the thieno[3,2-b]thiophene group have smaller V_{oc} losses than the devices employing CO*i*XDFIC NFAs centered with the benzene ring, and thus extending the core structure with thieno[3,2-b]thiophene groups can further reduce the V_{oc} loss. Furthermore, when HS was applied to cast the photoactive layer, while the V_{loss} of PTB7-Th:CO*i*5DFIC, PTB7-Th:CO*i*6DFIC and PTB7-Th:CO*i*7DFIC devices are similar to their RT-cast counterparts, the HS-cast PTB7-Th:CO*i*8DFIC device displays further reduced V_{oc} loss, implying that the charge separation process is facilitated in the PTB7-Th:CO*i*8DFIC device cast on HS [48].

Conclusion

In summary, we have systemically investigated the effects of the C-O-bridged ladder-type electron-

donating core structures of NFAs on their optical band gaps, molecular ordering and photovoltaic properties. Our results demonstrate that the thieno[3,2-b]thiophene-centered NFAs (CO*i*6DFIC and CO*i*8DFIC) possess narrower optical band gaps and broader absorption spectra compared to the benzene-centered NFAs (CO*i*5DFIC and CO*i*6DFIC). Meanwhile, with less fused rings in the core structure, both CO*i*5DFIC and CO*i*6DFIC exhibit edge-on oriented lamellar crystalline structures in their pure and blend films with PTB7-Th, a contrasting molecular orientation with the face-on PTB7-Th resulting in low device efficiency. For CO*i*7DFIC and CO*i*8DFIC, although the extended fused rings boosted the formation of backbone stacking in solid films which led to large aggregates of NFAs in pure films, the lamellar crystallization was reduced in CO*i*7DFIC-based films and completely suppressed in CO*i*8DFIC-based films by blending with PTB7-Th and using a hot substrate film-casting method. The chemical structure and film-processing conditions should be coordinated to fine tune the molecular ordering of NFAs containing the C-O-bridged core units to optimize the light absorption, exciton dissociation and charge transport processes to achieve the highest device performance.

Experimental

Experimental Section

CO*i*5DFIC, CO*i*6DFIC, CO*i*7DFIC and CO*i*8DFIC were synthesized as in our previous work [23]. PTB7-Th was purchased from Solarmer Materials (Beijing) Inc. ZnO precursor solution was prepared according to a previous literature report [49]. All solar cells were fabricated in an inverted structure. The prepatterned ITO-glass substrates (resistance ca. 15 Ω per square) were cleaned by sequential sonication in water, ethanol and isopropyl alcohol for 10 minutes each, before drying at 100 °C on a hotplate. These substrates were further treated with ultraviolet/ozone for 10 minutes before further use. 30 nm thick ZnO films were spin-coated onto cleaned ITO substrates, then dried at 200 °C for 30 min in air. The photoactive layer was then deposited on top of the ZnO layer by spin-coating from a 14 mg/ml chlorobenzene solution (with 0.5 vol.% DIO as additive) of PTB7-Th:CO*i*5DFIC, PTB7-Th:CO*i*6DFIC, PTB7-Th:CO*i*7DFIC, PTB7-Th:CO*i*8DFIC solutions with a donor:acceptor ratio of 1:1.5, in a nitrogen-filled glovebox. In order to achieve similar thicknesses of the active layer at 100 nm, the spin speed for devices cast at RT was chosen as 600 rpm. For devices cast on HS, the ITO/ZnO substrate were preheated on a hot plate held at 100 °C and quickly moved

to the chuck of a spin coater to spin-coat the photovoltaic solution at 1300 rpm. Then, for all devices, 10 nm MoO_3 and 100 nm Ag were thermally evaporated forming the anode and counter electrode under high vacuum to finish device preparation. The size of the photoactive area defined by the overlapping of anode and cathode is 4 mm^2.

Characterization

Film absorption spectra were measured using a UV-Visible spectrophotometer (Lambda750, Perkin, USA). Film thicknesses were measured using a spectroscopic ellipsometer (J. A. Woollam, USA). The surface morphologies of the active layers were characterized by scanning probe microscopy (NT-MDT, Russia) and transmission electron microscopy (JEOL, Japan). Device J-V characterization was performed under AM 1.5G illumination (100 mW cm^{-2}) using a Newport 3A solar simulator (USA) in air at room temperature. The light intensity was calibrated using a standard silicon reference cell certified by the National Renewable Energy Laboratory (USA). J-V characteristics were recorded using J-V sweep software developed by Ossila Ltd. (UK) and a Keithley 2612B (USA) source meter unit. External quantum efficiency was measured with an EQE system equipped with a standard Si diode (Zolix, China). Photoluminescence was obtained using a PL microscopic spectrometer (Flex One, Zolix, China) with a 532 nm CW laser as the excitation source. Synchrotron based grazing incidence wide angle X-ray scattering measurements were conducted at beamline I07 of Diamond Light Source in UK and data was analysed using FIT2D.

Acknowledgements

This work was supported by the National Natural Science Foundation of China (Grants No. 21774097) and the Natural Science Foundation of Hubei Province (Grant No. 2018CFA055). L. D. thanks National Key Research and Development Program of China (2017YFA0206600) and National Natural Science Foundation of China (U1401244, 51773045, 21772030, 21572041, 21704021 and 51503050) for financial support. We also that the UK STFC for part-funding this work via grant ST/R002754/1 “Synchrotron Techniques for African Research and Technology”, and EPSRC for funding studentships for R. C. K. and for E. L. K. S. and J. A. S. via the CDT in New and Sustainable Photovoltaics (EP/L01551X/1). The GIWAXS measurements reported here were performed on I07 at The Diamond Light Source (UK) on beam-time project reference S120419.

Reference

1 P. Chen, G. Li, X. Zhan, Y. Yang, *Nat. Photonics* **2018**, *12*, 131.

2 J. Hou, O. Inganas, R. H. Friend, F. Gao, *Nat. Mater.* **2018**, *17*, 119.

3 C. Yan, S. Barlow, Z. Wang, H. Yan, A. K. Y. Jen, S. R. Marder, X. Zhan, *Nat. Rev. Mat.* **2018**, *3*, 18003.

4 J. Zhao, H. S. Tan, X. Guo, A. Facchetti, H. Yan, *Nat. Energy* **2018**, *3*, 720.

5 S. Zhang, Y. Qin, J. Zhu, J. Hou, *Adv. Mater.* **2018**, *30*, 1800868.

6 H. Li, Z. Xiao, L. Ding, J. Wang, *Sci. Bull.* 2018, 63, 340.

7 J. Yuan, Y. Zhang, L. Zhou, G. Zhang, H. L. Yip, T. K. Lau, X. Lu, C. Zhu, H. Peng, P. A. Johnson, M. Leclerc, Y. Cao, J. Ulanski, Y. Li, Y. Zou, *Joule* **2019**, doi.org/10.1016/j.joule.2019.01.004.

8 L. Meng, Y. Zhang, X. Wan, C. Li, X. Zhang, Y. Wang, X. Ke, Z. Xiao, L. Ding, R. Xia, H. L. Yip, Y. Cao, Y. Chen, *Science* **2018**, *361*, 1094.

9 Y. Lin, J. Wang, Z. Zhang, H. Bai, Y. Li, D. Zhu, X. Zhan, *Adv. Mater.* **2015**, *27*, 1170.

10 S. Li, L. Zhan, F. Liu, J. Ren, M. Shi, C. Li, T. P. Russell, H. Chen, *Adv. Mater.* **2018**, *30*, 1705208.

11 W. Zhao, S. Li, H. Yao, S. Zhang, Y. Zhang, B. Yang, J. Hou, *J. Am. Chem. Soc.* **2017**, *139*, 7148.

12 B. Fan, X. Du, F. Liu, W. Zhong, L. Ying, R. Xie, X. Tang, K. An, J. Xin, N. Li, W. Ma, C. J. Brabec, F. Huang, Y. Cao, *Nat. Energy* **2018**, *3*, 1051.

13 S. Dai, T. Li, W. Wang, Y. Xiao, T. K. Lau, Z. Li, K. Liu, X. Lu, X. Zhan, *Adv. Mater.* **2018**, 30, 170651.

14 J. Sun, X. Ma, Z. Zhang, J. Yu, J. Zhou, X. Yin, L. Yang, R. Geng, R. Zhu, F. Zhang, W. Tang, *Adv. Mater.* **2018**, *30*, 1707150.

15 J. Wang, J. Zhang, Y. Xiao, T. Xiao, R. Zhu, C. Yan, Y. Fu, G. Lu, X. Lu, S. R. Marder, X. Zhan, *J. Am. Chem. Soc.* **2018**, *140*, 9140.

16 J. Zhu, Z. Ke, Q. Zhang, J. Wang, S. Dai, Y. Wu, Y. Xu, Y. Lin, W. Ma, W. You, X. Zhan, *Adv. Mater.* **2018**, *30*, 1704713.

17 J. Qu, H. Chen, J. Zhou, H. Lai, T. Liu, P. Chao, D. Li, Z. Xie, F. He, Y. Ma, *ACS Appl. Mater. Interfaces* **2018**, *10*, 39992.

18 S. Li, L. ye, W. Zhao, S. Zhang, S. Mukherjee, H. Ade, J. Hou, *Adv. Mater.* **2018**, *30*, 1704713.

19 N. Qiu, H. Zhang, X. Wan, C. Li, X. Ke, H. Feng, B. Kan, H. Zhang, Q. Zhang, Y. Lu, Y. Chen, *Adv. Mater.* **2018**, *29*, 1604964.

20 C. B. Nielsen, S. Holliday, H. Y. Chen, S. J. Cryer, I. McCulloch, *Acc. Chem. Res.* **2015**, *48*, 2803.

21 Y. Lin, X. Zhan, *Adv. Energy Mater.* **2015**, *5*, 1501063.

22 S. Li, W. Liu, C. Li, T. K. Lau, X. Lu, M. Shi, H. Chen, *J. Mater. Chem. A* **2016**, *4*, 14983.

23 W. Li, J. Cai, Y. Yan, F. Cai, S. Li, R. S. Gurney, D. Liu, J. D. McGettrick, T. M. Watson, Z. Li, A. J. Pearson, D. G. Lidzey, J. Hou, T. Wang, *Solar RRL* **2018**, *2*, 1800114.

24 J. Mai, Y. Xiao, G. Zhou, J. Wang, J. Zhu, N. Zhao, X. Zhan, X. Lu, *Adv. Mater.* **2018**, *30*, 1802888.

25 L. Ye, W. Zhao, S. Li, S. Mukherjee, J. H. Carpenter, O. Awartani, X. Jiao, J. Hou, H. Ade, *Adv. Energy Mater.* **2017**, *7*, 1602000.

26 Y. Huang, E. J. Kramer, A. J. Heeger, G. C. Bazan, *Chem. Rev.* **2014**, *114*, 7006.

27 X. Song, N. Gasparini, L. Ye, H. Yao, J. Hou, H. Ade, D. Baran, *ACS Energy Lett.* **2018**, *3*, 669.

28 L. Ye, H. Hu, M. Ghasemi, T. Wang, B. A. Collins, J. H. Kim, K. Jiang, J. H. Carpenter, H. Li, Z. Li, T. McAfee, J. Zhao, X. Chen, J. L. Y. Lai, T. Ma, J. L. Bredas, H. Yan, H. Ade, *Nat. Mater.* **2018**, *17*, 253.

29 B. A. Gregg, *J. Phys. Chem. Lett.* **2011**, *2*, 3013.

30 R. S. Gurney, D. G. Lidzey, T. Wang, *Rep. Prog. Phys.* **2019**, *82*, 036601.

31 W. Li, M. Chen, J. Cai, E. L. K. Spooner, H. Zhang, R. S. Gurney, D. Liu, Z. Xiao, D. G. Lidzey, L. Ding, T. Wang, *Joule*, **2019**, DOI:10.1016/j.joule.2018.11.023.

32 R. S. Gurney, W. Li, Y. Yan, D. Liu, A. J. Pearson, T. Wang, *J. Energy Chem.* **2019**, *37*, 148.

33 R. Yu, H. Yao, L. Hong, Y. Xu, B. Gao, J. Zhu, Y. Zu, J. Hou, *Nat. Commun.* **2018**，*9*，4645.

34 N. Wang, L. Zhan, S. Li, M. Shi, T. K. Lau, X. Lu, R. Shikler, C. Z. Li, H. Chen, *Mater. Chem. Front.* **2018**, *2*, 2006.

35 L. Ye, S. Li, X. Liu, S. Zhang, M. Ghasemi, Y. Xiong, J. Hou, H. Ade, *Joule* **2019**, doi.org/10.1016/j.joule.2018.11.006.

36 T. Li, H. Zhang, Z. Xiao, J. J. Rech, H. Niu, W. You, L. Ding, *Mater. Chem. Front.* **2018**, *2*, 700.

37 K. Jin, C. Deng, L. Zhang, D. Li, T. Li, F. Wang, Y. Yuan, Z. Xiao, L. Ding, *Mater. Chem. Front.* **2018**, *2*, 1716.

38 Z. Xiao, X. Jia, D. Li, S. Wang, X. Geng, F. Liu, J. Chen, S. Yang, T. P. Russell, L. Ding, *Sci. Bulletin.* **2017**, *62*, 1494.

39 L. Zhang, K. Jin, Z. Xiao, X. Wang, T. Wang, C. Yi, L. Ding, *Mater. Chem. Front.* **2019**, 3, 492-495.

40 Z. Xiao, S. Yang, Z. Yang, J. Yang, H. L. Yip, F. Zhang, F. He, T. Wang, J. Wang, Y. Yuan, H. Yang, M. Wang, L. Ding, *Adv. Mater.* **2019**, 1804790.

41 W. Li, M. Chen, Z. Zhang, J. Cai, H. Zhang, R. S. Gurney, D. Liu, J. Yu, W. Tang, T. Wang, *Adv. Funct. Mater.* **2019**, *29*, 1807662.

42 G. Li, Y. Yao, H. Yang, V. Shrotriya, G. Yang, Y. Yang, *Adv. Funct. Mater.* **2007**, *17*, 1636.

43 S. Li, L. Zhang, W. Zhao, S. Zhang, B. Ali, Z. Fu, T. K. Lau, X. Lu, M. Shi, C. Z. Li, J. Hou, H. Chen, *J. Mater. Chem. A*, **2018**, *6*, 12132.

44 S. M. Swick, W. Zhu, M. Matta, T. J. Aldrich, A. Harbuzaru, J. T. L. Navarrete, R. P. Ortiz, K. L. Kohlstedt, G. C. Schatz, A. Facchetti, F. S. Melkonyan, T. J. Marks, *Proc. Natl. Acad. Sci. U S A* **2018**, E8341.

45 T. M. Clarke, J. R. Durrant. *Chem. Rev.* **2010**, *110*, 6736.

46 E. F. Palermo, S. B. Darling, A. J. McNeil, *J. Mater. Chem. C* **2014**, *2*, 3401.

47 Y. Wang, D. Qian, Y. Cui, H. Zhang, J. Hou, K. Vandewal, T. Kirchartz, F. Gao, *Adv. Energy Mater.* **2018**, 1801352.

48 J. Liu, S. Chen, D. Qian, B. Gautam, G. Yang, J. Zhao, J. Bergqvist, F. Zhang, W. Ma, H. Ade, O. Inganäs, K. Gundogdu, F. Gao, H. Yan, *Nat. Energy* **2016**, *1*, 16089.

49 Y. Sun, J. Seo, C. J. Takacs, J. Seifter, A. J. Heeger, *Adv. Mater.* **2011**, *23*, 1679.